





MultiCAM: a multivariable framework for connecting the mass accretion history of haloes with their properties

Ismael Mendoza ^{1,★} Philip Mansfield ^{2,3} Kuan Wang ^{1,4} and Camille Avestruz ^{1,4}

¹Department of Physics, The University of Michigan, Ann Arbor, MI 48109 USA

²Kavli Institute of Particle Astrophysics and Cosmology, Stanford University, Stanford, CA 94305, USA

³SLAC National Accelerator Laboratory, Menlo Park, CA 94025, USA

⁴Leinweber Center for Theoretical Physics, University of Michigan, 450 Church St, Ann Arbor, MI 48109, USA

Accepted 2023 May 16. in original form 2023 February 15

ABSTRACT

Models that connect galaxy and halo properties often summarize a halo’s mass accretion history (MAH) with a single value, and use this value as the basis for predictions. However, a single-value summary fails to capture the complexity of MAHs and information can be lost in the process. We present *MultiCAM*, a generalization of traditional abundance matching frameworks, which can simultaneously connect the full MAH of a halo with multiple halo and/or galaxy properties. As a first case study, we apply MultiCAM to the problem of connecting dark matter halo properties to their MAHs in the context of a dark matter-only simulation. While some halo properties, such as concentration, are more strongly correlated to the early-time mass growth of a halo, others, like the virial ratio, have stronger correlations with late-time mass growth. This highlights the necessity of considering the impact of the entire MAH on halo properties. For most of the halo properties we consider, we find that MultiCAM models that use the full MAH achieve higher accuracy than conditional abundance matching models that use a single epoch. We also demonstrate an extension of MultiCAM that captures the covariance between predicted halo properties. This extension provides a baseline model for applications where the covariance between predicted properties is important.

Key words: methods: numerical – galaxies: clusters: general – galaxies: evolution – galaxies: haloes – dark matter

1 INTRODUCTION

Characterizing the properties and growth of dark matter haloes has been an important goal of cosmological *N*-body simulations (Diemand & Moore 2011; Frenk & White 2012). Dark matter haloes are groups of dark matter particles that have gravitationally collapsed into bound structures. In the Λ CDM cosmological model, every galaxy forms within the potential well provided by a dark matter halo (White & Rees 1978; Blumenthal et al. 1984). Thus, galaxies and their dark matter haloes are closely connected, meaning that models which attempt to predict the properties of galaxies must account for the behaviour and properties of their dark matter haloes (e.g. Hearin & Watson 2013; Hearin et al. 2016; Wechsler & Tinker 2018).

Previous work has established a deep connection between a halo’s present-day ($z = 0$) properties and its *mass accretion history* (MAH), i.e. its mass growth as a function of time. Properties such as concentration, virial ratio, centre of mass offset, spin, axis ratio, and splash-back radius have been studied in relation to MAH. Early-forming haloes tend to have a higher concentration on average than late-forming haloes (e.g. Wechsler et al. 2002), and merger events induce lasting changes in halo structure which are encoded as a universal signatures in the halo’s concentration (e.g. Wang et al. 2020). Other properties like the centre of mass offset, virial ratio, and splashback radius have strong correlations with the halo’s recent mass growth

history and merging activity (e.g. Power et al. 2012; Shin & Diemer 2023). This joint dependence leads to substantial covariance between halo parameters (e.g. Lau et al. 2021). Much of this dependence comes from long-term growth trends: it has been found that a significant percentage of the variance in the concentration, axis ratio, and spin of a dark matter halo can be explained by the first principal component of the mass assembly history (e.g. Chen et al. 2020).

The MAH of a halo directly impacts the dynamical state of a halo, which in turn determines the reliability of structural measurements of its properties. Previous studies have established that haloes that have recently experienced one or more major mergers are more likely out of dynamical equilibrium (Tormen et al. 1997; Hetzner & Burkert 2006). These major merger events can cause temporary deviations from a halo’s equilibrium state during which its structural properties change rapidly and might not be well defined (Ludlow et al. 2016). Thus, it is critical that we characterize the dynamical state of haloes so that their structural measurements can be robustly propagated to downstream analysis. Previous work measuring the distribution of halo properties in simulations attempted to address this by selecting a subsample of *relaxed haloes*, i.e., those haloes considered to be close to dynamical equilibrium (e.g. Neto et al. 2007; Klypin et al. 2011, 2016). A closely related line of work seeks to identify relaxed galaxy clusters to avoid similar biases in the corresponding measurements (e.g. Cui et al. 2017; Zhang et al. 2022). However, there is a significant ambiguity on how to exactly define this relaxed sample for both cases, which usually rely on hard-cuts. This further highlights the need for

★ E-mail: imendoza@umich.edu

Parameter	Value
Box size	250 Mpc h^{-1}
Number of particles	2048 ³
Particle mass	$1.35 \times 10^8 M_{\odot} h^{-1}$
Force resolution	1.0 kpc h^{-1}
Initial redshift	80
Number of snapshots	180
Hubble parameter h	0.7
Ω_{Λ}	0.73
Ω_m	0.27
Ω_b	0.0469
Tilt n	0.95
σ_8	0.82

Table 1. Simulation and cosmological parameters of the Bolshoi dark matter-only cosmological Λ CDM simulation presented in [Klypin et al. \(2011\)](#), which is based on the WMAP5 cosmology ([Dunkley et al. 2009](#)).

increasing our understanding of the relationships between a galaxy’s or halo’s properties, MAH, and dynamical state.

A common way to connect galaxy or halo properties to their MAH is to use a single parameter summary of the MAH, such as the half-mass scale (e.g. [Gao et al. 2005](#)) or the value returned by a single-parameter fit (e.g. [Wechsler et al. 2002](#)). This framework leads to a one-to-one parameter correlation analysis called abundance matching, which corresponds to a prediction model that *assumes perfect correlation* between the two parameters (e.g. half-mass scale and halo concentration) ([Kravtsov et al. 2004](#)). Abundance matching and its hierarchical extension, conditional abundance matching (CAM, [Hearin et al. 2014](#), see Section 3.3.1 for a description of these methods), have been effective models for a range of applications. For example, CAM can predict low-redshift galaxy statistics like two-point correlation functions in SDSS to reasonable accuracy ([Hearin et al. 2014](#)). However, the MAH of a dark matter halo is a complex multidimensional quantity that contains richer predictive information than single parameter summaries.

MAHs are typically made up of a smooth accretion component consisting of an early-fast accretion phase and a late-slow accretion phase, which was successfully captured with a three-parameter model in ([Hearin et al. 2021](#)). The MAH also includes a non-smooth accretion component in the form of an arbitrary number of discrete major merger events that can significantly change halo properties on a short time-scale (e.g. [Hetznecker & Burkert 2006](#); [Power et al. 2012](#); [Wang et al. 2020](#)). Separately, it has been shown that different present-day halo properties correlate more or less strongly with different parts of the MAH (e.g. [Wong & Taylor 2012](#)). Thus, summarizing the MAH with a single quantity leads to discarding a significant amount of useful information. Another significant drawback of one-to-one parameter models is that they are unable to capture the covariance between predictions. If the same single parameter MAH summary is chosen, CAM-like models necessarily output a perfect correlation between any pair of predicted halo properties. Thus, if one is interested in emulating multiple halo properties from a given MAH, one-to-one models are insufficient.

To address the aforementioned limitations we propose a new method for connecting galaxy or halo properties with their formation history: *MultiCAM*. MultiCAM is a generalization of the traditional abundance matching framework that consistently incorporates the full formation history into a prediction of single-epoch properties while preserving the key benefits of CAM. MultiCAM utilizes the full covariance between features and targets in its predictions. Moreover, MultiCAM can predict multiple properties simultaneously and correctly capture the correlations between them. As a first demonstration of our new method, we apply it to connecting dark matter halo properties with their MAH. In the future, our main focus will be in applying this method to predict baryonic properties.

This paper is organized as follows. Section 2 describes the simulation suite and halo sample used in our studies. Section 3 presents the parametrizations of MAH we consider in this work, gives an overview of CAM, and a detailed description of MultiCAM. In Section 4 we characterize the covariance of MAH and halo present-day properties, and evaluate MultiCAM on our halo sample. Section 5 discusses future applications of MultiCAM and how it compares to other methods. Finally, in Section 6 we present our conclusions.

2 DATA SET

2.1 Simulation suite

For our data set we use the Bolshoi dark matter-only cosmological simulation ([Klypin et al. 2011](#)) which was performed with the Adaptive-Refinement-Tree (ART) code described in ([Kravtsov et al. 1997](#)). The simulation has outputs at 180 snapshots starting at $a_{179} = 0.07835$ and ending at $a_0 = 1.00035 \approx 1$. The spacing between early snapshots is $\Delta a = 0.006$ between $a_{179} = 0.07835$ and $a_{77} = 0.80835$, and $\Delta a = 0.003$ between late snapshots $a_{77} = 0.80835$ and $a_0 = 1.00035$. The cosmological parameters and other simulation details are shown in Table 1.

The halo catalogues were generated by the ROCKSTAR halo finder ([Behroozi et al. 2013a](#)), as run by [Rodríguez-Puebla et al. \(2016\)](#). This catalogue uses both position and velocity information to identify each halo in the simulation. Halo finder comparison projects have found this algorithm to perform well at halo finding tasks, including detecting substructure and tracing mergers (e.g., [Knebe et al. 2011](#)).

We use catalogues generated by CONSISTENT-TREES ([Behroozi et al. 2013b](#)) to construct the merger history that we use for our analysis ([Rodríguez-Puebla et al. 2016](#)). Given a merger event, we define the *main progenitor* halo as the one that contains the most particles that end up in the resulting halo after the merger. Given a present-day ($z = 0$) halo, a *merger tree* can be constructed by following its evolution at each snapshot in the simulation going backwards in time. The *main progenitor branch* of a given present-day halo is the branch in the merger tree resulting from following the main progenitor halo backwards in time at each snapshot.

2.2 Defining the halo sample

Throughout this work we use the same data set of a random sample of 10,000 haloes from the Bolshoi simulation in the mass bin of $M_{\text{vir}} \in [10^{12}, 10^{12.2}] h^{-1} M_{\odot}$ which we denote as M12. Here, M_{vir} is the bound mass within a radius enclosing an average density corresponding to the overdensity threshold defined in [Bryan & Norman \(1998\)](#). We take this radius to be the virial radius R_{vir} .

For each of the haloes in this sample, we use the ROCKSTAR catalogue at each snapshot and CONSISTENT-TREES to extract the corre-

sponding main progenitor branch and the virial masses of progenitors at each snapshot in this branch. We do not use all of the 180 snapshots in the Bolshoi simulation, rather we impose a cut-off based on the mass resolution of our simulation. We pick our first snapshot to be the earliest snapshot out of the 180 where at most 5% of haloes have a virial mass lower than 50 times the particle mass. This ensures that we never attempt to analyse snapshots where a substantial portion of our sample is unresolved. For our M12 sample, we consider a total of $N_{\text{snap}} = 165$ scales ranging from $a_{164} = 0.18635$ up to $a_0 = 1$.

For the small percentage $\leq 1\%$ of haloes in our sample that do not have a corresponding main line progenitor at a_{164} (or in any subsequent snapshots), we assign them a virial mass at those missing snapshots to be the mass of a single particle of the simulation. This is so that there are no missing values in the MAHs for all haloes in our M12 sample.

2.3 Halo properties and their convergence

In this study we mainly consider halo concentration, c_{vir} , defined as the ratio of the virial radius to the NFW scale radius; the normalized maximum value of the halo's rotation curve $V_{\text{max}}/V_{\text{vir}}$; the offset between the halo's centre of mass and its most bound particle x_{off} ; the virial ratio, $T/|U|$; its dimensionless spin parameter, λ_{bullock} ; and its second minor-to-major axis ratio, c/a . See [Mansfield & Avestruz \(2021\)](#) for the exact definitions of these properties as computed by ROCKSTAR.

[Mansfield & Avestruz \(2021\)](#) measured the minimum converged masses for each of these properties in Bolshoi at different levels of acceptable numerical bias. No detectable bias is measured in $V_{\text{max}}/V_{\text{vir}}$ at $M_{\text{vir}} > 10^{11.8} h^{-1} M_{\odot}$ at $M_{\text{vir}} > 10^{11.6} h^{-1} M_{\odot}$, $T/|U|$ at $M_{\text{vir}} > 10^{11.1} h^{-1} M_{\odot}$, λ_{bullock} at $M_{\text{vir}} > 10^{10.2} h^{-1} M_{\odot}$, and c/a at $M_{\text{vir}} > 10^{10.9} h^{-1} M_{\odot}$. [Mansfield & Avestruz \(2021\)](#) do not report a c_{vir} convergence limit for Bolshoi, but do report a c_{vir} convergence limit for Erebus_CBoL_L125 ([Diemer & Kravtsov 2015](#)) at $M_{\text{vir}} > 10^{11.6} h^{-1} M_{\odot}$, which has an identical cosmology, identical particle mass, coarser force softening, and coarser time-steps than Bolshoi. Therefore, all the considered properties are converged within our mass window of $[10^{12}, 10^{12.2}] h^{-1} M_{\odot}$.

We also briefly consider several other, more minor halo properties. For example, the average of the first minor-to-major axis ratio b/a and the second minor-to-major ratio c/a , which we denote with q :

$$q = \frac{1}{2} \left(\frac{b}{a} + \frac{c}{a} \right).$$

Because this property is derived from b/a and c/a , it is converged at about $10^{10.9} h^{-1} M_{\odot}$. For all other halo properties, their definitions can be found in [Mansfield & Avestruz \(2021\)](#) and they are also converged within our mass window.

3 METHODS

3.1 Parametrizations of MAHs

First, we introduce the notation that we use to parametrize the MAHs and their properties. We measure time through the cosmological scale factor:

$$a(z) = \frac{1}{1+z} \quad (1)$$

We track mass growth through the normalized peak mass,

$$m(a) = \frac{M_{\text{peak}}(a)}{M_{\text{peak}}(a=1)}, \quad (2)$$

where we take the ratio of M_{peak} values to force monotonicity,

$$M_{\text{peak}}(a) = \max_{0 \leq a' \leq a} [M_{\text{vir}}(a')]. \quad (3)$$

The difference between $M_{\text{peak}}(a)$ and $M_{\text{vir}}(a)$ is significant for sub-haloes due to the large amount of mass loss they experience (e.g. [Wechsler & Tinker 2018](#)), but the difference is less important for the central haloes in M12, since their masses will typically increase over time. The main impact on our sample of host haloes is that it allows $m(a)$ to be inverted. To that end, we define

$$a(m) = m(a)^{-1}. \quad (4)$$

Since $m(a)$ is monotonic, but not strictly increasing, we take $a(m)$ to be the first scale factor at which the halo reaches a given mass. When inverting $m(a)$ we use piecewise power-law interpolation between adjacent snapshots of a halo's MAH.

In addition, per convention, we sometimes use the notation $a_{1/n}$ where n is an integer to mean:

$$a_{1/n} = a(m = 1/n). \quad (5)$$

This notation, usually with $n = 2$, is often used in the literature as a tracer of formation (e.g. [Gao et al. 2005](#)).

We define a halo's dynamical time t_{dyn} as the time it takes for a test particle to travel a distance of virial radius R_{vir} at a speed of V_{vir} , the orbital speed of a particle on a circular orbit at R_{vir} . Since all haloes have the same enclosed density within R_{vir} , t_{dyn} is only a function of redshift and cosmology:

$$t_{\text{dyn}} = \frac{R_{\text{vir}}}{\sqrt{GM_{\text{vir}}/R_{\text{vir}}}} = \frac{1}{H(z)} \left(\frac{2\rho_c(z)}{\rho_{\text{vir}}(z)} \right)^{1/2} \quad (6)$$

$$= 2.01 \text{ Gyr} \left(\frac{\rho_{\text{vir}}(z)/\rho_c(z)}{97.0} \right)^{-1/2} \left(\frac{H(z)}{70 \text{ km s}^{-1} \text{ Mpc}^{-1}} \right)^{-1}. \quad (7)$$

For convenience, equation (7) is normalized to the $z = 0$ virial density in the Bolshoi simulation. Following from this definition, $m_{t_{\text{dyn}}}$ is the mass fraction at a time t_{dyn} before the present day. $m_{t_{\text{dyn}}}$ is a commonly used measure of late-time accretion rates and its unnormalized equivalent is tracked by CONSISTENT-TREES catalogues by default.

We also analyse the best-fitting exponential scale factor of each MAH ([Wechsler et al. 2002](#)):

$$M_{\text{vir}}(z)/M_{\text{vir}}(z=0) = e^{-\alpha z}. \quad (8)$$

3.2 DiffMAH model of smooth MAHs

We also consider the best-fitting parameters of the DiffMAH model of smooth MAHs presented in [Hearin et al. \(2021\)](#). This model consists of the following fitting function:

$$M_{\text{peak}}(t)/M_{\text{peak}}(t=t_0) = (t/t_0)^{\alpha(t)} \quad (9)$$

where t is age of the universe, and t_0 is the present-day age of the universe. Finally, $\alpha(t)$ is a sigmoid function defined as:

$$\alpha(t; \tau_c, k, \alpha_{\text{early}}, \alpha_{\text{late}}) \equiv \alpha_{\text{early}} + \frac{\alpha_{\text{late}} - \alpha_{\text{early}}}{1 + \exp(-k(t - \tau_c))} \quad (10)$$

and has parameters α_{early} , α_{late} , k , and τ_c with an explicit physical meaning. First, α_{early} , α_{late} determine the asymptotic value of the power-law index at early and late times respectively; τ_c controls the transition time between the early- and late-time indices; and k determines the speed of transition between the two phases. As in [Hearin et al. \(2021\)](#), we fix $k = 3.5$.

M : Number of Features Lower half quantiles
 T : Number of Targets Upper half quantiles

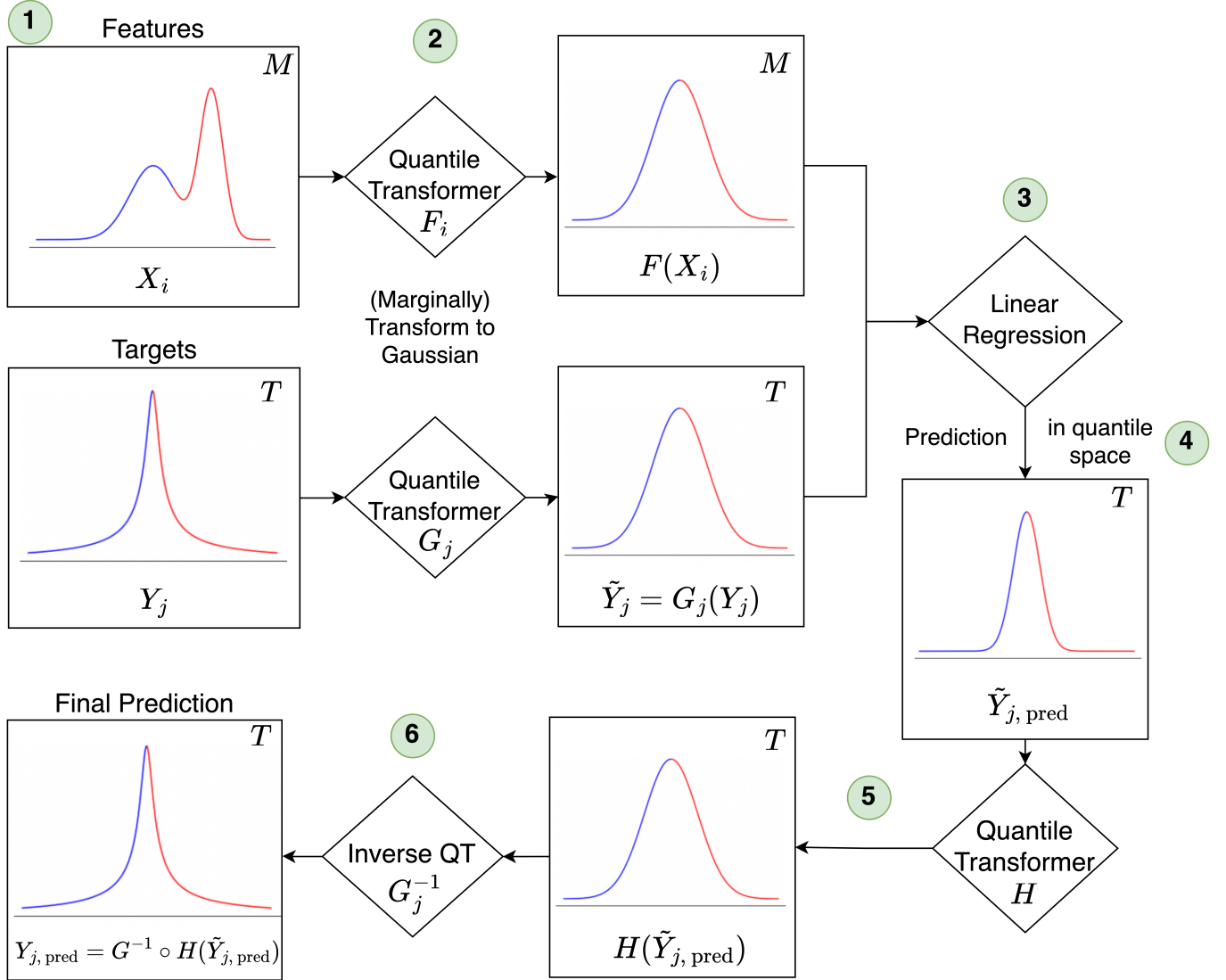


Figure 1. Schematic illustrating the MultiCAM method. In this diagram we illustrate the novel method presented in this work to connect MAH information to present-day halo properties: ‘MultiCAM’. Each step of our algorithm is marked with a green circle. Each box represents the 1D distribution of one of the M features or T targets. The curve of each 1D distribution is delineated so that the blue and red curves intersect at the median. The rhombuses represent algorithms, either a quantile transformer to marginally map variables to Gaussian distributions, or a linear regression prediction model. The algorithm and each of the steps are described in detail in Section 3.3.2.

3.3 Statistical algorithms

In this section we introduce the statistical algorithms we use for predictions connecting MAH and present-day halo properties.

3.3.1 Conditional abundance matching

One of the methods we use is an adapted *Conditional-Abundance Matching (CAM)*. The CAM algorithm is a method which was originally developed to study and model the connection between halo ages — traced through properties like $a_{1/2}$ — to observable galaxy properties — like galaxy colour or star formation rate (Hearin & Watson 2013; Hearin et al. 2014; Watson et al. 2015). It is simi-

lar to the traditional abundance matching algorithm (Kravtsov et al. 2004), which assigns stellar masses or luminosities to simulated dark matter haloes. Traditional abundance matching evaluates the function $N_{\star}^{-1}(N_{\text{dm}}(M_{\text{vir}}))$, where N_{\star} and N_{dm} are some observed cumulative stellar mass function and theoretical cumulative mass function, respectively. Similarly, CAM assigns galaxy properties via $F_{\text{gal}}^{-1}(F_{\text{halo}}(X_{\text{mah}}|M_{\star})|M_{\star})$, where F_{halo} and F_{gal} are the conditional CDFs at a fixed stellar mass M_{\star} for some theoretical tracer of halo age, X_{mah} , and the CDF for the target observable galaxy property, respectively.

The primary application of CAM is generating empirical models of observable properties. But more generally, CAM is a method that

optimally implements a specific assumption for the connection between halo growth and halo/galaxy properties: a given halo property Y_{halo} is entirely and monotonically determined by a given feature of a halo's MAH X_{mah} . If this assumption is correct, CAM predictions will be the exact values of the given halo property, and failures in this assumption propagate into inaccuracies in CAM predictions. Therefore, throughout this paper, we use the CAM prediction strength as a measure of how well a given halo property Y_{halo} can be understood to be determined by a given proxy of halo growth X_{mah} . Moreover, multi-parameter models which have improved predictive power over CAM are evidence that the halo property in question is influenced by multiple features in a halo's MAH.

In this work, the CAM algorithm is used to abundance match a given MAH feature X_{mah} to a given present-day halo property Y_{halo} , at fixed present-day halo mass M_{vir} . Specifically with the equation:

$$Y_{\text{halo}} = F_{\text{halo}}^{-1}(F_{\text{mah}}(X_{\text{mah}}|M_{\text{vir}})|M_{\text{vir}}) \quad (11)$$

where F_{halo} and F_{mah} are the conditional CDF of the present-day halo property and the MAH feature respectively. Throughout, we condition at a fixed mass bin equal to the one used for constructing the M12 data set.

We pick the MAH property X_{mah} for abundance matching to be the scale $a(m_{\text{opt}})$ (see equation 4) at a fixed mass bin m_{opt} that optimally correlates with Y_{halo} across all m . For example, when $Y_{\text{halo}} = c_{\text{vir}}$, we find $m_{\text{opt}} \approx 0.5$ in our M12 data set, so that $X_{\text{mah}} = a(m_{\text{opt}}) \approx a(0.5) = a_{1/2}$. The optimal mass bin m_{opt} satisfies the equation:

$$\max(\rho_{\text{sp}}(a(m), Y_{\text{halo}})) = \rho_{\text{sp}}(a(m_{\text{opt}}), Y_{\text{halo}}). \quad (12)$$

Similarly, we could have chosen $X_{\text{mah}} = m(a_{\text{opt}})$ where the optimal scale a_{opt} satisfies:

$$\max(\rho_{\text{sp}}(m(a), Y_{\text{halo}})) = \rho_{\text{sp}}(m(a_{\text{opt}}), Y_{\text{halo}}), \quad (13)$$

but we find that $a(m_{\text{opt}})$ has overall higher correlations across all halo properties than $m(a_{\text{opt}})$. We refer to the algorithm that uses $a(m_{\text{opt}})$ to abundance match between MAH and halo properties at a given halo mass as 'CAM $a(m_{\text{opt}})$ '. We use CAM $a(m_{\text{opt}})$ to predict a given halo property Y_{halo} from the MAH of a halo in Section 4.3.

CAM is a simple, yet powerful empirical non-parametric approach to matching any pair of strongly correlated variables. It however has some important limitations: (1) It is unable to match multiple variables to another set of multiple variables. (2) It does not incorporate the scatter between prediction and target when matching. We address these limitations of CAM in the algorithms described next.

3.3.2 MultiCAM

We propose the new algorithm *MultiCAM* to address these limitations of CAM. MultiCAM generalizes CAM to match multiple MAH properties to multiple present-day halo properties simultaneously. To accomplish this, MultiCAM first introduces a multi-variable linear regression between the multiple features and target variables. Then, MultiCAM marginally matches the distribution of outputs to the true distribution of targets. In our context, different halo properties correlate more or less strongly at different time scales of a halo's growth history (e.g. Wong & Taylor 2012). This means that matching multiple variables consistently is essential for exploring the connections in this work.

MultiCAM also includes a pre-processing step where all features and target variables are marginally transformed to Gaussian distributions. At the end of the procedure, all variables are transformed to their original space. This pre-processing step is beneficial in the context of linear regression since it allows for a version of MultiCAM

that introduces scatter between the features and targets, as discussed in detail in Sections 3.3.3 and 3.3.4.

The MultiCAM algorithm is illustrated in Fig. 1 and in detail consists of the following:

(i) Collect all desired features for prediction, X , and targets, Y , from a given data set. For example, X can be set to the full MAH of all haloes in the data set: $X_{\text{mah}} = \{a(m_i)\}_{i=1}^N$, where $\{m_i\}_{i=1}^N$ are some pre-defined mass bins with $m_N = 1$. Similarly, Y can be set to all the halo present-day properties we consider in this work $Y_{\text{halo}} = \{c_{\text{vir}}, T/|U|, x_{\text{off}}, \lambda_{\text{bullock}}, c/a\}$, which are described in Section 2.3.

(ii) We marginally transform each individual feature from its empirical distribution to a normal distribution (top left of figure) to a Gaussian distribution. We do this via the inverse transform method (e.g. Devroye 1986), which can map any 1D data set of variables to have any other desired empirical distribution without changing the rank-ordering of its points.

(iii) We then take the subset of marginalized Gaussian features \tilde{X}_{train} and targets \tilde{Y}_{train} in the training set, and train a linear regression model for prediction in this Gaussianized space for these features and targets.

(iv) We then use the marginalized Gaussian features in the testing set \tilde{X}_{test} and apply linear regression to obtain the corresponding set of predictions \tilde{Y}_{pred} .

(v) The predictions from the linear regression model \tilde{Y}_{pred} are not guaranteed to follow the distribution of transformed targets (they tend to be narrower). Thus, we apply one more quantile transformer to \tilde{Y}_{pred} and make its distribution (marginally) Gaussian, which then matches the distribution of the Gaussianized training targets \tilde{Y}_{train} . This is illustrated in the bottom-left corner of Fig. 1.

(vi) Finally, we transform the Gaussianized predictions \tilde{Y}_{pred} back into original target space by applying the inverse of the original quantile transformer used to map training target variables to the Gaussianized space. The result is the final MultiCAM prediction Y_{pred} .

This approach incorporates the multi-variable prediction accuracy from linear regression while preserving the properties of the marginal predictor distributions. Due to the quantile transformations illustrated in Fig. 1, our procedure automatically outputs predictions whose marginal distributions match the marginal distributions of the training data. This means that the outputs from MultiCAM have a correlation strength with the true targets that is at least as high as CAM (see Section 4.2). In fact, MultiCAM exactly reduces to CAM in the case of 1D features and targets. In summary, MultiCAM also has the added advantage of (1) predicting multiple target properties from multiple input properties and (2) taking advantage of the increased accuracy from linear regression.

This version of MultiCAM that uses linear regression still faces one key limitation in that it doesn't account for the scatter between features and targets, and thus will not reproduce the correct correlations between output properties. To address this, we first discuss the relationship between linear regression and sampling from a conditional Gaussian. Second, we discuss a method that maintains the correlation between sampled properties that is based on using conditional Gaussian sampling within MultiCAM instead of linear regression.

3.3.3 Linear regression and conditional Gaussian sampling

We start by discussing the theoretical framework of conditional Gaussian prediction, and then connect it with linear regression and Multi-

CAM. Assume that you have some multi-dimensional features X and multi-dimensional targets Y that are jointly distributed as a multivariate Gaussian $P_{X,Y}$. Given a new feature test point x^* , we consider the conditional distribution $P_{Y|x^*}$ in order to choose our new prediction based on x^* . The conditional distribution $P_{Y|x^*}$ is also Gaussian with mean $\bar{\mu}(x^*)$ and covariance matrix $\bar{\Sigma}$. The equations to derive the conditional parameters $\bar{\mu}(x^*)$ and $\bar{\Sigma}$ from empirical estimates of the joint distribution $P_{X,Y}$ parameters can be found in Appendix A.

Given this framework, there are two different goals we could choose to pursue: (1) Minimize (squared) residuals of the prediction $Y_{\text{pred}}(X)$ relative to the target Y or (2) Sample points Y such that their distribution matches the true target distribution $P(Y)$, including in its correlations between different target variables.

The first goal is achieved by using the mode of the conditional distribution directly as the prediction:

$$y_{\text{pred}}(x^*) \equiv \bar{\mu}(x^*). \quad (14)$$

Based on the expression for $\bar{\mu}(x^*)$ in equation (A5), we can see how this prediction would not take into account the intrinsic scatter of the target distribution, as there is no term with Σ_{yy} – the covariance matrix between target variables.

The second goal can be achieved by sampling the conditional distribution $P_{Y|X}$ after sampling $P(X)$. Concretely, given a test point $x^* \sim P(X)$, we choose as our prediction samples directly from the conditional normal distribution $P_{Y|x^*}$:

$$y_{\text{pred}}(x^*) \sim \mathcal{N}(\bar{\mu}(x^*), \bar{\Sigma}). \quad (15)$$

This second approach does incorporate the intrinsic scatter in the target distribution as $\bar{\Sigma}$ depends on Σ_{yy} , as can be seen in equation (A6) in Appendix A. We denote this approach *conditional Gaussian sampling*.

In Appendix B, we prove that the mode of the conditional distribution $P_{Y|X}$ (equation 14) is equivalent to the linear regression output if X, Y are jointly normal distributed. Additionally, MultiCAM already includes a pre-processing step (step 2 of the algorithm in Section 3.3.2) where we try to bring features X and targets Y close to a joint Gaussian. These two facts combined imply that the conditional Gaussian sampling approach (equation 15) is a natural replacement for the linear regression prediction algorithm within MultiCAM that could allow us to account for the scatter between targets.

Finally, note that we restrict analysis in this paper to simulation data, where we can train the entirety of Σ and account for the explicit covariance between all features and predicted quantities. However, conditional Gaussian sampling provides an avenue to use MultiCAM as an interpretable empirical model. In the simplest case, if we consider traditional CAM as such an empirical model, the “fit” procedure would consist of Σ containing one row for X_{mah} , one row for the target galaxy observable, and off-diagonal terms artificially fixed to assume perfect correlation. In the more general case using MultiCAM with conditional Gaussian sampling, we would perform an analogous “fit” procedure by taking any subset of the elements in Σ as free parameters.

3.3.4 MultiCAM with scatter

As mentioned previously, the MultiCAM algorithm presented in Section 3.3.2 cannot correctly capture the correlation between targets. As explained in Section 3.3.3 this is because the prediction model connecting features and targets, linear regression, does not account for the scatter in the target distribution.

However, given that the MultiCAM algorithm presented in Section 3.3.2 already includes a normalizing pre-processing step (step

Model	$x_{\text{off}}, \lambda_{\text{bullock}}$	$x_{\text{off}}, c/a$	$\lambda_{\text{bullock}}, c/a$
True	0.51	-0.43	-0.29
CAM $a(m_{\text{opt}})$	0.62	-0.79	-0.88
MultiCAM (no scatter)	0.93	-0.96	-0.95
MultiCAM (with scatter)	0.50	-0.45	-0.31

Table 2. Correlations between halo properties predicted from each model.

We show the Spearman correlation between each pair of predicted target $z = 0$ halo properties given their MAH using three different methods. The training and testing (‘True’) data sets are equivalent to the one used for Fig. 2 in Section 3.3.4.

2), we can replace the prediction model from linear regression (step 3 and 4) to conditional Gaussian sampling (equation 15) to solve this problem. As explained in Section 3.3.3, the pre-processing step allows us to interpret this replacement as using the same joint normal distribution to solve a different goal, that of directly sampling $P(Y)$. This can be achieved by using the conditional Gaussian sampling approach within MultiCAM, since we will be explicitly incorporating the scatter between targets in our predictions. Therefore, for the rest of this subsection, we denote this new version of MultiCAM as *MultiCAM (with scatter)* to distinguish it from the method in Section 3.3.2 which we will denote as *MultiCAM (no scatter)*. Unless otherwise stated, in the rest of the paper ‘MultiCAM’ refers to ‘MultiCAM (no scatter)’.

Importantly, the MultiCAM (with scatter) approach explicitly models scatter between features and targets, i.e. a given test data point of features can be used to sample multiple predictions from the conditional normal distribution. This means that the point estimate accuracy of MultiCAM (with scatter) will be lower compared to MultiCAM (no scatter), since we are introducing noise into the prediction. However, we will show how this simple extension allows for capturing the lion’s share of the covariance between variables while still matching the marginal distributions exactly.

To demonstrate this, we first train each of the models presented so far — CAM $a(m_{\text{opt}})$, MultiCAM (no scatter), and MultiCAM (with scatter) — on 7000 random haloes from the M12 data set using the full MAH $\{a(m_i)\}_{i=1}^N$ of each halo as features and three present-day halo properties as targets: c/a , λ_{bullock} , and x_{off} . The three models are then tested on full MAH of remaining 3000 haloes from the M12 data set and the 2D, 1σ , 2σ , and 3σ contours between each pair of target predicted variables are plotted as shown in Fig. 2. The true contours are shown in orange and the predicted contours by each model in green.

In Fig. 2, we see that CAM $a(m_{\text{opt}})$ and MultiCAM (no scatter) fail to match the 2D distributions of halo properties. For CAM $a(m_{\text{opt}})$, the width of the green contours in each panel directly corresponds to the covariance between the $a(m_{\text{opt}})$ of each property, since CAM does a one-to-one matching between these. For example, x_{off} and λ_{bullock} are the target variables with the largest difference in their corresponding m_{opt} , as shown in Table 3. Fig. 3 demonstrates that a larger difference in mass bins m between a pair of scales $a(m)$ implies a lower covariance between them. Thus, we expect a weaker correlation between the CAM $a(m_{\text{opt}})$ -predicted x_{off} and λ_{bullock} than for the other pairs of variables. This is exactly what we see in the leftmost subplot in Fig. 2. MultiCAM (no scatter) has the narrowest contours out of the three methods. This is because the predicted variables use the same sets of MAHs and there is substantial overlap in the relative importance of different epochs (see Section 4.2).

However, MultiCAM (with scatter) has contours that seem to match the true contours more closely.

Additionally, Table 2 shows the correlation between each pair of $z = 0$ halo properties for each of the three models. We can quantitatively reach the same conclusions suggested by Fig. 2: the correlations between target properties outputted by MultiCAM (with scatter) agree closely with the true correlations, but this is not the case for CAM $a(m_{\text{opt}})$ and MultiCAM (no scatter).

The full triangle plot applying MultiCAM (with scatter) to the main present-day properties considered in this work is shown in Fig. C1 of Appendix C, which shows good agreement in both 1D marginals and 2D contours. As explained in Section 3.3.3, MultiCAM (with scatter) can successfully capture the covariance between target variables since the sampling scatter depends directly on this covariance (equation 15).

In summary, Table 2, Fig. 2, and Fig. C1 demonstrate that MultiCAM (with scatter) can be used to successfully emulate present-day halo properties given the full MAH of a dark matter halo.

4 RESULTS

In this section, we focus on understanding the statistical properties of our M12 data set through correlations and evaluate the MultiCAM approach. We choose to focus on the following $z = 0$ halo properties for our analysis: concentration, c_{vir} , virial ratio, $T/|U|$, centre of mass displacement, x_{off} , spin Bullock, λ_{bullock} , and second minor-axis to major-axis ratio, c/a .

We analyse the M12 data set as defined in Section 2. We divide the M12 halo sample into a training set of 7000 haloes and a test set of 3000 haloes (unless otherwise stated). The performance metrics of trained models are evaluated only on the test set. The error bars reported in all our results are standard errors estimated from jackknife resampling over 8 equal volume subcubes of the simulation.

4.1 Autocorrelation of halo MAHs

Fig. 3 shows 2D histograms where we colour code each pixel (bin) by Spearman correlation strength. The top plot shows the Spearman correlation, $\rho_{\text{sp}}(m(a_i), m(a_j))$, between mass fraction at a given pair of formation times. The bottom plot shows the Spearman correlation, $\rho_{\text{sp}}(a(m_i), a(m_j))$, between the formation time at a given pair of mass fractions in our M12 data set.

In the top panel, we see that $m(a)$ values are strongly correlated with one another for small ($\Delta a \approx 0.1$) changes in a . Similarly, in the bottom plot we see that $a(m)$ values are strongly correlated with one another for small ($\Delta m \approx 0.1$) changes in m . This suggests that we can achieve a similar prediction accuracy with a sparser subset of the MAH information. For example, if we wanted to retain information at a level of $\rho_{\text{sp}} \sim 0.9$ between adjacent bins, we could choose data at approximately a spacing of $\Delta a = 0.05$ which would result in approximately ten times less data.

Another takeaway from the top plot is that adjacent snapshots at both early and late times are strongly correlated (see Section 2.1). The distinct output cadence of Bolshoi should therefore have minimal impact in the following analysis.

The takeaways for the bottom plot are similar to those from the top plot.

4.2 Correlations of MAH and present-day halo properties

In Fig. 4, we show the Spearman correlation coefficient between several present-day halo properties and the halo accretion history, parametrized as $m(a)$ (left) and $a(m)$ (right). We compute the correlation using all 10,000 haloes in our M12 sample. The coloured red bands correspond to the uncertainty on each curve as estimated by jackknife resampling. In this figure, solid lines are used to represent positive correlation values and dotted lines represent negative values.

Both figures illustrate that present-day halo properties contain information about the growth of haloes back to very early times, $z \approx 4$, and at times when haloes were $\approx 10\%$ to 20% of their current mass. As expected, formation times correlate positively with c_{vir} (Wechsler et al. 2002), $V_{\text{max}}/V_{\text{vir}}$ (this follows directly from the c_{vir} correlation with growth), c/a (Allgood et al. 2006; Chen et al. 2019), and negatively with $T/|U|$, x_{off} (Maccio et al. 2007), and λ_{bullock} (Vitvitska et al. 2002).

Inner halo structure, tracked by c_{vir} and $V_{\text{max}}/V_{\text{vir}}$, most strongly correlates with early times, $\approx 3.4\tau_{\text{dyn}}$ in the past, when haloes were roughly half their current mass. This is consistent with models of halo structure in which the inner profile is primarily set by long term growth trends (e.g. Dalal et al. 2010; Ludlow et al. 2013). More recently, Wang et al. (2020) systematically examined the correlation between the present-day concentration and different stages of halo mass assembly. They found that there are extended periods in the assembly history that correlate strongly with the present-day halo structure, which justifies the use of various definitions of halo formation time with which to predict present-day concentrations. These findings are qualitatively consistent with our results.

The other properties that we track, x_{off} , $T/|U|$, λ_{bullock} , and c/a have relatively larger predictive power at late times compared with properties that more closely describe the halo inner structure, such as c_{vir} . All four are expected to be tracers of dynamically unrelaxed haloes that have recently experienced major mergers or rapid, anisotropic smooth accretion from nearby filaments. More relaxed haloes will be more spherical, more centred on its most bound point, and will have a virial ratio closer to 0.5 (Mo et al. 2010). Any deviations would be caused by recent external influences, which are typically mergers for non-subhaloes (although mass loss due to tidal stripping can also influence halo properties, e.g., Tucci et al. 2021). The correlation with spin is generally understood to arise because a slowly accreting halo will generally accrete isotropically, reducing its normalized angular momentum over time, while a rapidly accreting halo will experience larger mergers which will inject large amounts of angular momentum into the system (e.g. Vitvitska et al. 2002). However, halo spin also plays a large role in the early collapse of dark matter perturbations prior to forming haloes (e.g. Sheth et al. 2001), meaning that it should not be thought of as a purely late-time phenomenon.

Table 3 contains the values of optimal correlations between halo properties and MAH which correspond to the peaks of the curves in Fig. 4. As an example, we include a dashed vertical line in the left-hand panel of Fig. 4 which intersects the peak of the correlation curve for the $V_{\text{max}}/V_{\text{vir}}$ property. In other words, the x -value of the vertical orange line is a_{opt} when $X = V_{\text{max}}/V_{\text{vir}}$, which corresponds to the second row of Table 3.

We also measured correlations with other measures of triaxiality, q and semi-minor axis ratio b/a . The a_{opt} of q and the ellipticity ratio c/a are the same, but q has a slightly higher peak absolute Spearman correlation with MAH of $|\rho_{\text{sp}}| = 0.533$ compared to $|\rho_{\text{sp}}| = 0.510$ for c/a . The correlation between b/a and MAH is comparable with that between c/a and MAH.

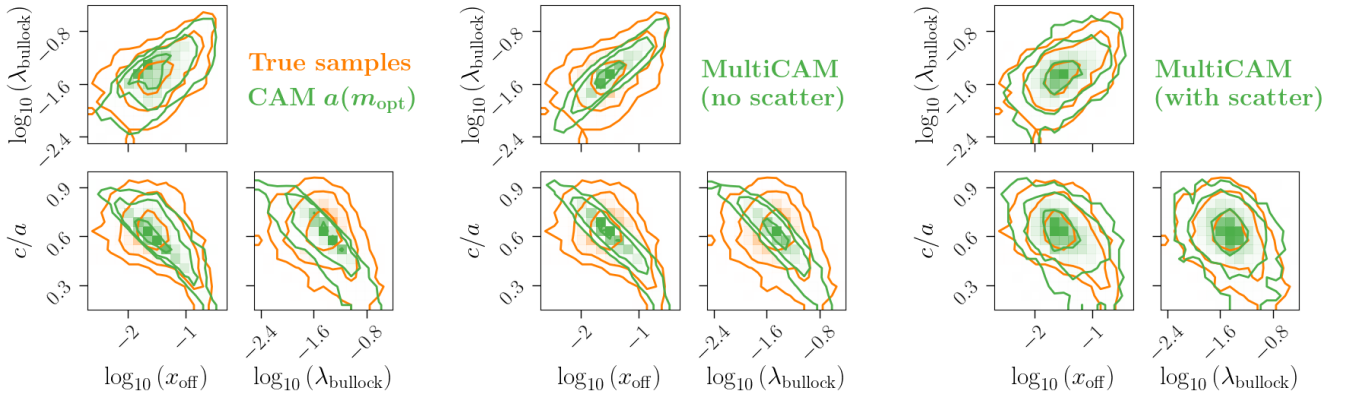


Figure 2. 2D Scatter with contours from samples of $z = 0$ halo properties comparing different models. We show plots of 1σ , 2σ , and 3σ contours for the 2D histograms of 3000 samples of $z = 0$ halo properties given their MAH using three different methods. Each method is applied to λ_{bullock} , c/a , and x_{off} within our M12 data set. The orange contours in each subplot show the true empirical distributions of these properties. The green contours of each subplot were produced by applying three different prediction methods to these halo properties: CAM $a(m_{\text{opt}})$ (left), MultiCAM with no scatter (middle), and MultiCAM with scatter (right). These models were trained on the remainder of the M12 data set. For more details on the different methods used, see Section 3.3, and for more discussion on the figure see Section 3.3.4.

Analogously, we evaluated the results for λ_{Peebles} , the Peebles spin parameter. This measurement was comparable with λ_{Bullock} , but λ_{Bullock} has a higher peak correlation of $\rho_{\text{sp}} = 0.473$ compared to λ_{Peebles} , which has a peak correlation of $\rho_{\text{sp}} = 0.384$, likely due to the fact that measurements of internal energy for λ_{Peebles} are less stable leading to weaker signals. We use λ_{Bullock} in all subsequent analyses considering the spin of the haloes.

In comparing $V_{\text{max}}/V_{\text{vir}}$ to c_{vir} , the peak correlation occurs slightly earlier in the former quantity with comparable correlation strength.

Finally, we note that the correlation between $m(a)$ and present-day properties drops for both very early times and late times (left side of Fig. 4). The former drop is because halo properties across the board are no longer correlated with those early times. The latter drop is related to the distribution of $m(a)$ at later times. The limiting behaviour of all $m(a)$ curves is to approach 1 as a approaches 1. This means that the limiting behaviour of the scatter in $m(a)$ is to approach zero as a approaches 1 and, conversely, to grow as a decreases. This trend of decreasing scatter in $m(a)$ with increasing a is explained by the fact that once a halo reaches or exceeds its present-day mass, $m(a)$ becomes fixed to 1 for the rest of that halo's history (see equation 2). However, if we think of $m(a)$ as an accretion rate between the a and the present-day mass, as the time range over which the accretion rate is measured decreases, the intrinsic noise in that measurement becomes larger. The width of $m(a)$ eventually becomes smaller than this intrinsic noise in $m(a)$, thus decreasing the correlation. The cause of the drop in correlation between $a(m)$ and the halo properties (right side of Fig. 4) at very low and very high mass fractions stems from a similar argument.

4.3 Predictions of present-day properties based on MAH

In Fig. 5, we show the Spearman correlation between several predicted halo properties and their true value for four different models described in Section 3.3.

In blue circles, we show results for our canonical MultiCAM model, using the full MAH of each halo. Under this metric, Mul-

tiCAM either outperforms or performs comparably well to the other tested models.

With orange squares, we show results of applying MultiCAM to the best-fitting DiffMAH curve for each MAH (see Section 3.2 for more information). This model is next in predictive power for the target halo properties shown. We highlight the similar performance between this model and MultiCAM trained on the full non-parametrized MAH (blue circles) for most halo properties. The consistency of performance implies that our method leans heavily on information contained within the smooth accretion history.

Next, we show the performance of a model that applies MultiCAM to the three best-fitting parameters from DiffMAH in green diamonds. We note that the DiffMAH parameters alone have systematically lower prediction power than the full MAH curve that the DiffMAH parameters describe. This may be due to the non-linear mapping of DiffMAH parameters onto the MAHs that cannot be captured by the linear modelling we employ in MultiCAM. Further investigation might include testing non-linear models to map DiffMAH parameters to halo properties.

Relatedly, the decrease in prediction power for MultiCAM on DiffMAH parameters suggests a degeneracy between DiffMAH parameters and present-day halo properties. In that case, the exact parametrization of the DiffMAH curve matters. Indeed, one can show from equations 9 and 10 that we can pick a parametrization where we replace α_{early} with $a_{1/2}$ and still get a complete set of DiffMAH parameters that uniquely characterizes a MAH curve. We find an increase of ≥ 0.05 in the correlation with c_{vir} , λ_{bullock} , and c/a with this alternative parametrization. This indicates that the DiffMAH parametrization chosen impacts the predictive power of DiffMAH parameters, which is also further evidence of the aforementioned degeneracy.

Finally, in the purple pluses, we show model predictions for CAM evaluated at a_{opt} , which only uses the scale at a single mass fraction of a halo that best correlates with that halo property (see Table 3). We see that MultiCAM on the full MAH significantly outperforms CAM $a(m_{\text{opt}})$ for prediction of most halo properties including: c_{vir} , $T/|U|$, and x_{off} . For the other two halo properties, λ_{bullock} and c/a , Multi-

X	a_{opt}	$\rho_{\text{sp}}(X, m(a_{\text{opt}}))$	m_{opt}	$\rho_{\text{sp}}(X, a(m_{\text{opt}}))$
c_{vir}	0.420 ± 0.006	0.677 ± 0.005	0.495 ± 0.021	-0.698 ± 0.006
$V_{\text{max}}/V_{\text{vir}}$	0.384 ± 0.018	0.683 ± 0.004	0.397 ± 0.051	-0.700 ± 0.006
$V_{\text{off}}/V_{\text{vir}}$	0.616 ± 0.040	-0.523 ± 0.008	0.735 ± 0.036	0.574 ± 0.008
x_{off}	0.652 ± 0.007	-0.551 ± 0.007	0.735 ± 0.032	0.599 ± 0.012
$T/ U $	0.562 ± 0.052	-0.588 ± 0.010	0.673 ± 0.082	0.623 ± 0.011
λ_{peebles}	0.480 ± 0.010	-0.342 ± 0.007	0.541 ± 0.023	0.384 ± 0.007
λ_{bullock}	0.480 ± 0.007	-0.430 ± 0.006	0.541 ± 0.023	0.473 ± 0.007
c/a	0.580 ± 0.025	0.465 ± 0.006	0.644 ± 0.033	-0.510 ± 0.006
b/a	0.592 ± 0.006	0.460 ± 0.008	0.673 ± 0.029	-0.505 ± 0.008
q	0.580 ± 0.022	0.487 ± 0.006	0.673 ± 0.033	-0.533 ± 0.007
R_{200m}/R_{vir}	0.544 ± 0.008	-0.367 ± 0.007	0.292 ± 0.045	0.321 ± 0.008
R_{500c}/R_{vir}	0.532 ± 0.011	0.593 ± 0.011	0.673 ± 0.029	-0.614 ± 0.011

Table 3. Optimal correlations between present-day halo properties and single-epoch measurements of the MAH. In this table we show the optimal scale factors, a_{opt} , and mass fractions, m_{opt} , at which the present-day halo properties of our halo sample achieve their maximum absolute Spearman correlation with $m(a)$ or $a(m)$ respectively. These values correspond to the maxima of the curves in Fig. 4. The precise definition of m_{opt} and a_{opt} can be found in Section 3.1.

CAM and CAM $a(m_{\text{opt}})$ have (statistically) the same performance. Moreover, CAM performs significantly better than MultiCAM on DiffMAH parameters, which might be related to the fact that CAM a_{opt} is using (by construction) the best single feature in predicting MAH.

Comparing the individual models within different types of halo properties, we notice a few trends. First, the full curve from the DiffMAH fit performs at least as well as the model trained with CAM a_{opt} on all halo properties. The MultiCAM on DiffMAH fit information provides better predictions on properties that are most strongly correlated with overall MAH, e.g. c_{vir} and $T/|U|$. For properties whose predicted values are more weakly correlated with truth (i.e. λ_{Bullock} and c/a), all models, except for the one using the DiffMAH parameters only, perform similarly.

The halo property predictions where CAM applied to a_{opt} perform comparably well tend to be in the “worst” cases of target predictions (e.g. x_{off} , λ_{Bullock} , and c/a). We surmise that the comparable performance is due to the fact that these halo properties are largely dependent on the most recent MAH of the haloes and that these properties are even more sensitive to the non-smooth component of the MAH, comprised of moderate and major mergers, which our model does not yet account for.

We additionally investigated whether using the gradient of the MAH could successfully capture the missing major merger information. Specifically, we computed the first-order derivative of MAHs using a Savitzky–Golay Filter (Savitzky & Golay 1964) and used these derivatives as additional features for MultiCAM. However, we found no significant difference between MultiCAM trained on the full MAH and its gradients compared to our canonical MultiCAM model trained only on the full MAH.

4.4 Predictions of MAH summaries based on present-day properties

In Fig. 6 we use MultiCAM to perform the inverse of the test shown in Fig. 5: predicting summary statistics of a halo’s MAH from its $z = 0$ halo properties. We attempt to predict $a_{1/2}$, the half-mass

scale (equation 5), α , the characteristic time in an exponential MAH fit (equation 8), $m(t_{\text{dyn}})$, the accretion rate over a dynamical time (equation 2), and the three DiffMAH parameters, τ_c , α_{late} , and α_{early} (equations 9 and 10). We use MultiCAM to predict these values with different combinations of c_{vir} , $T/|U|$, x_{off} , λ_{bullock} , and c/a .

Using MultiCAM on the full suite of halo properties (purple plus signs) results in strictly more accurate predictions than using a single halo property, as expected. As expected from Fig. 4, c_{vir} (blue circles) does a better job predicting tracers of early accretion history like $a_{1/2}$, α , and α_{early} than x_{off} (orange squares) and $T/|U|$ (green diamonds). The opposite is true for tracers of late accretion history, like $m(t_{\text{dyn}})$ and α_{late} .

Simpler parametrizations, like α for an exponential growth history, are well-predicted, but for more complicated non-linear parameters like in the DiffMAH fits, predictions are quite poor. This is most likely due to the degeneracy between DiffMAH parameters and halo properties as discussed in Section 4.3.

Despite being comparatively poorly predicted, the same trends can be seen in the DiffMAH parameters that are seen in the single-epoch MAH tracers. α_{late} encodes behaviour at late times and is better predicted by x_{off} and $T/|U|$ than by c_{vir} . τ_c is sensitive to earlier times and better predicted by c_{vir} than x_{off} and $T/|U|$. α_{early} probes even earlier times and shows no statistically significant trends. This may either be due to α_{early} having a relatively small impact on the overall MAH or it corresponding to such an early time period that no present-day properties do a good job at tracing it.

In Fig. 7 we use MultiCAM with the same models as in Fig. 6 to predict the full MAH either with the $m(a)$ parametrization (left) or the $a(m)$ parametrization (right). We use the same scale and mass bins for prediction as in Fig. 4 which consist of the Bolshoi simulation cadences for $m(a)$ (left) and uniformly spaced log bins on m between 0 and 1 for $a(m)$ (right). For each parametrization, we show the Spearman correlation coefficient between predicted MAH and true MAH of our test set from the M12 data set.

MultiCAM with all properties (purple diamonds) produces strictly more accurate predictions for the mass-accretion histories of haloes

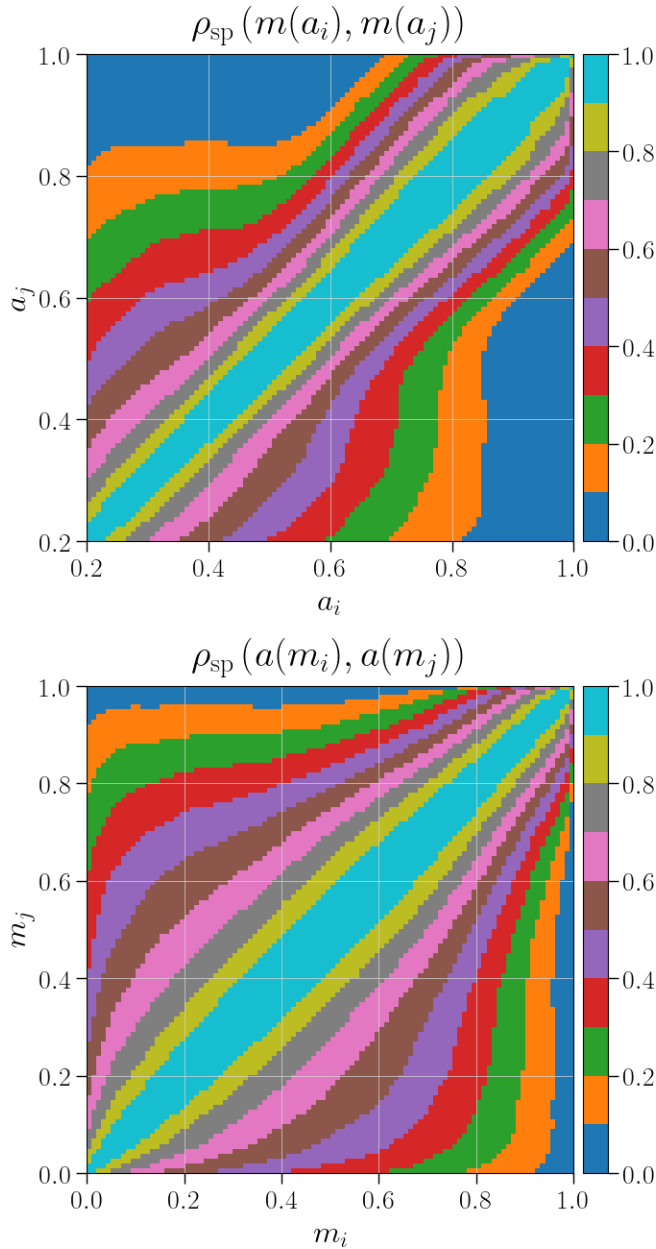


Figure 3. Internal MAH Spearman correlation. The colour in each 2D bin (pixel) of these plots corresponds to the Spearman correlation $\rho_{\text{sp}}(m(a_i), m(a_j))$ between the mass fraction at a given pair of formation times, (a_i, a_j) (top), and the Spearman correlation $\rho_{\text{sp}}(a(m_i), a(m_j))$ between the formation time at a given pair of mass fractions, (m_i, m_j) (bottom), for all the 10000 haloes in our M12 data set. See Section 4.2 for additional discussion.

than any individual property. It leverages properties like c_{vir} to maintain high accuracy ($\rho_{\text{spearman}} \approx 0.75$) at early times and switches to later-time properties like $T/|U|$ and x_{off} to maintain that accuracy after c_{vir} ceases to be a good tracer of growth.

Overall, the curves follow the same trends as in Fig. 4. For example, x_{off} and $T/|U|$ are better at predicting late history than c_{vir} . $T/|U|$ has higher correlation than x_{off} throughout. This is expected since higher Spearman correlation corresponds to higher prediction power. For the same reason as in Fig. 4, all models predictive power drop at very early and very late times.

Finally, as discussed in Section 3.3.2, MultiCAM reduces to CAM

in the case of connecting a single feature with a single target variable. This means that the MultiCAM predicted correlations for the models using a single halo property as a feature in Fig. 6 and Fig. 7 are equivalent to the CAM predictions for the corresponding MAH summary.

5 DISCUSSION

In this work, we have studied the correlations between a halo's present-day properties and multiple intermediate epochs of their MAH. In particular, we investigated the time and mass scales at which different halo properties correlate most strongly with the MAH (see Fig. 4 and Table 3). We find a significant non-zero correlation between all the halo properties we studied and its formation history for most time and mass scales, with most halo properties, including concentration, achieving their strongest correlation with the MAH at intermediate time and mass scales. This is in disagreement with the findings in Wong & Taylor (2012), where the authors find that correlation between concentration and the MAH was strongest when the halo had accumulated only 20% of its mass for a relaxed halo sample. However, we see a high level of agreement both quantitatively and qualitatively for the correlation between concentration and MAH with Wang et al. (2020) and Shin & Diemer (2023), who both use the same halo finder (ROCKSTAR) as our work. We thus hypothesize that the disagreement with Wong & Taylor (2012) is due to differences in halo finder and halo sample, but leave confirmation of this for future work.

We also studied the autocorrelations between different epochs of mass growth. Fig. 3 shows that a sparser representation of the MAH can provide a similar amount of predictive information to model galaxy or halo properties. This conclusion is similar to the one reached in Wong & Taylor (2012), where their principal component analysis of MAHs suggested that only a few principal components explained the majority of the scatter in the MAHs. Physically, this indicates that longer time-scales of mass accretion likely set halo properties.

Our model and subsequent analysis adds to a growing body of literature that models the connections between galaxies, dark matter haloes, and their MAHs (Wechsler & Tinker 2018). Such models have ranged from one-to-one mappings of properties in the form of abundance matching (Kravtsov et al. 2004), to complex machine-learning approaches (e.g. Machado Poletti Valle et al. 2021; Hausen et al. 2023; Horowitz et al. 2022; Stiskalek et al. 2022; de Andres et al. 2023). We provide a generalization of CAM and quantify its ability to connect halo properties with their full MAH. Other recent models enable connections between more details of a halo's full MAH with corresponding halo or galaxy properties. For example, Jespersen et al. (2022) builds a graph neural network that directly uses the full dark matter merger tree of a halo to accurately emulate galaxy properties and their scatter. They find that using the full formation history always outperforms predictions compared to only using the $z = 0$ halo properties and a traditional abundance matching approach, which is consistent with our conclusions in Fig. 5 and Fig. 6. As another example, Lucie-Smith et al. (2022) uses gradient-boosted-tree algorithms to predict the final mass profiles of cluster-sized haloes based on the initial density field and the MAH. Their model is able to identify time-scales in the MAHs that are most predictive of the final mass profiles. Even though ML approaches such as Jespersen et al. (2022) are inherently non-linear and can achieve high prediction accuracy, MultiCAM allows for easily determining which subset of features contribute toward prediction power and is simpler to invert.

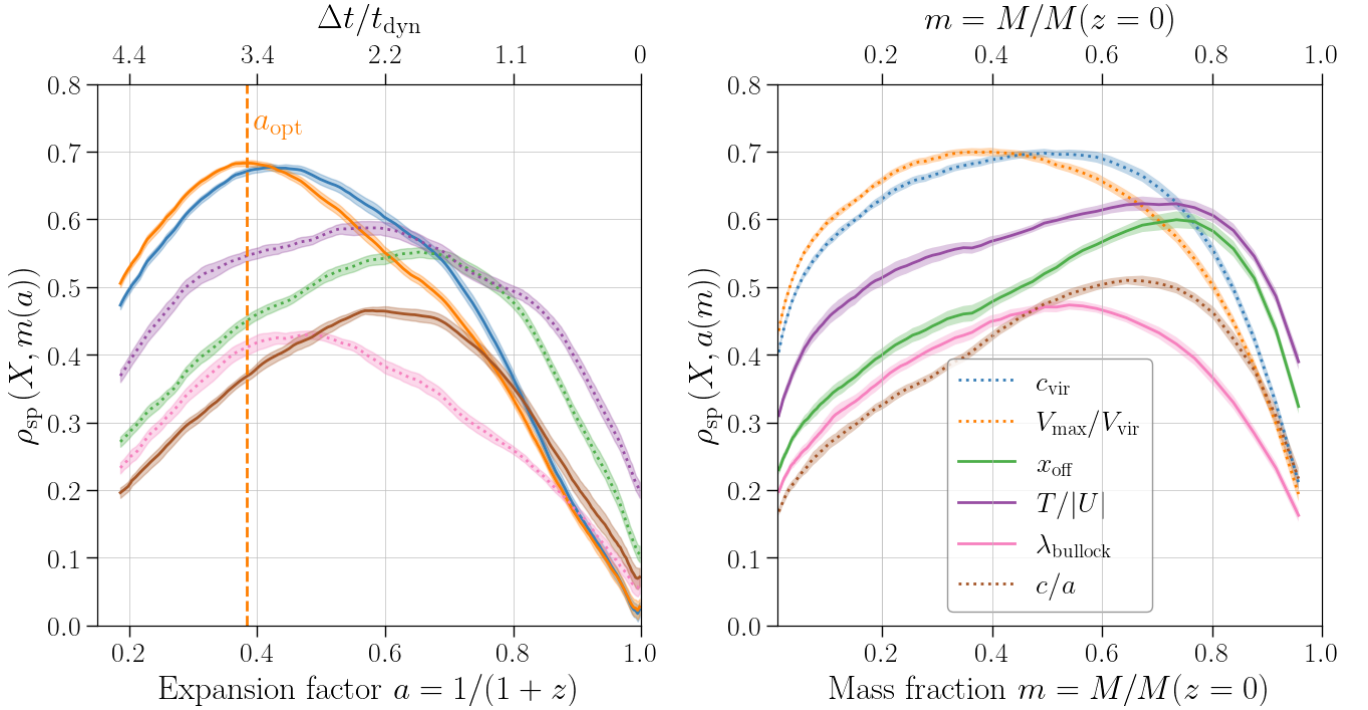


Figure 4. Correlation of accretion history with present-day properties. We show the Spearman correlation coefficient between different present-day halo properties, X , and accretion history, parametrized as $m(a)$ or $a(m)$. The correlation is calculated based on our complete 10000 halo sample M12. The coloured bands around each curve show the error estimated by jackknife resampling. In both figures, solid lines indicate positive correlation value and dotted lines indicate negative correlation value. See Section 4.2 for additional discussion on these plots. See Table 3 for the specific values of optimal correlations between halo properties and MAH (peaks in these plots). The annotated orange dashed vertical line in the left-hand plot illustrates one such optimal correlation a_{opt} for the $V_{\text{max}}/V_{\text{vir}}$ property (whose exact value is the second row in Table 3).

As demonstrated in Wang et al. (2020) and Rey et al. (2019), one major source of scatter in the concentration mass relation comes from mergers, and the scatter depends on fine grained details of these mergers. However, Fig. 4 shows that the last dynamical time of the halo is not providing much predictive information. This suggests that MultiCAM is not able to successfully extract the relevant merger and non-smooth information from the MAH features given. In addition, we attempted to capture merger information by incorporating gradient features of MAH in MultiCAM’s prediction. We found that the prediction performance of MultiCAM remained the same when adding these additional features across all halo properties. We therefore plan to explicitly incorporate major merger information from merger trees in future development and studies with MultiCAM.

Additional future applications of our method include (1) applying MultiCAM to connecting DM halo accretion histories to baryonic properties in the context of hydrodynamical simulations such as the THE300 project (Haggar et al. 2021), (2) using MultiCAM to build fast emulators that paste small-scale properties into cheaply generated ensembles of accurate mock halo catalogues (e.g. Tassev et al. 2013; Feng et al. 2016), or parametric models of MAHs (e.g. Hearin et al. 2021), (3) exploring other extensions of MultiCAM that incorporate more advanced non-linear methods, such as neural networks, that could provide higher predictive accuracy, and (4) applying MultiCAM as an empirical method where we can constrain the internal covariance matrix of the model with observational data.

Finally, previous work indicates that the MAHs closely connect to proxies for the dynamical state of galaxies, galaxy clusters, and their host haloes (e.g. Hetzner & Burkert 2006; Gouin et al. 2021). An improved understanding of this connection can better inform the interpretation of measurements of galaxy and galaxy cluster properties

(e.g. Ludlow et al. 2012; Mantz et al. 2015; Ludlow et al. 2016). The flexibility of MultiCAM provides a simple and interpretable framework to explore various measures of the dynamical state of DM haloes, galaxies, or galaxy clusters and to see how their dynamical state connects with their structural properties and accretion history. Specifically, MultiCAM provides a framework to study the predictive power of any combination of galaxy or halo properties on the MAH. Such studies could enable optimal combinations of properties that strongly correlate with merger information or other indicators of dynamical state. Thus, MultiCAM complements approaches to classifying the dynamical state of haloes or galaxies similar to the ones proposed in works such as De Luca et al. (2021) and Vallés-Pérez et al. (2023), which attempt to construct tracers of halo relaxedness from multiple halo properties.

6 CONCLUSION

In this study, we present MultiCAM, a generalization of traditional abundance matching algorithms. MultiCAM connects halo and galaxy properties with their MAHs. As a case study, we apply MultiCAM to connect the present-day properties of dark matter haloes with their full MAHs using the Bolshoi dark matter-only cosmological simulation.

Our key result is that we can use the entire MAH with MultiCAM to significantly outperform CAM in such connections. Our MultiCAM models are particularly successful in connecting the entire MAH with halo properties often used to trace MAH, such as c_{vir} , $T/|U|$, and x_{off} . For other halo properties considered (e.g. λ_{bullock}), MultiCAM

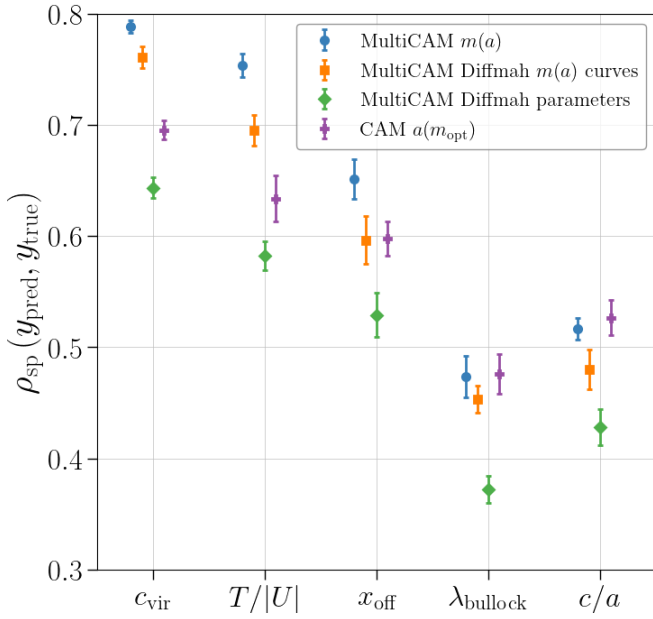


Figure 5. Correlation between predictions of $z = 0$ halo properties based on MAH and true properties. We show the Spearman correlation between several true $z = 0$ halo properties and predicted $z = 0$ halo properties using four trained models on the M12 data set. The first three models are based on MultiCAM trained on full MAH (blue circle), on DiffMAH curve fits to the MAH curves evaluated at the same scale factors as the full MAH (orange square), and on the parameters of the DiffMAH fit (green diamond). The last model (purple plus) is the prediction of the CAM algorithm using the corresponding $a(m_{\text{opt}})$ (defined in equation 12) for each halo property. See Section 4.3 for additional discussion on this figure.

performs at least as well as CAM. See Fig. 5 and Fig. 6 for relevant figures.

Our other main results are the following:

(i) There is a significant autocorrelation in dark matter haloes’ MAH. We find that values of normalized peak masses $m(a)$ are strongly correlated with one another for small changes in a . This indicates that a subset, or a sparser representation of MAH, might be sufficient to model some galaxy or halo properties with comparable information content. For more details, see Fig. 3.

(ii) The entire formation history of a halo leaves imprints on present-day properties. We find that all the properties in our subset of present-day halo properties have significant non-zero correlations with their MAH between $z \approx 4$ and $z = 0$. See Fig. 4.

(iii) We find that MultiCAM applied to the DiffMAH smooth parametrization of MAH (Hearin et al. 2021) performs comparably with MultiCAM applied on the full MAH for halo properties known to be strongly correlated with late-time merger events such as x_{off} and λ_{bullock} . This suggests that MultiCAM is not able to fully capture merger information in detail, which we leave for future work. See Fig. 5 for more details.

(iv) We show how a simple extension of MultiCAM based on conditional Gaussian sampling is able to simultaneously sample multiple halo properties based on the MAH and *capture the true correlation between properties*. See Fig. 2 and Fig. C1.

(v) Finally, we apply MultiCAM to the inverse problem of predicting the MAH of a halo from its present-day properties. We show that c_{vir} is better at predicting the early formation history of a halo, and $T/|U|$ and x_{off} are better at predicting the late-time formation history. MultiCAM enables simultaneous use of all halo properties for

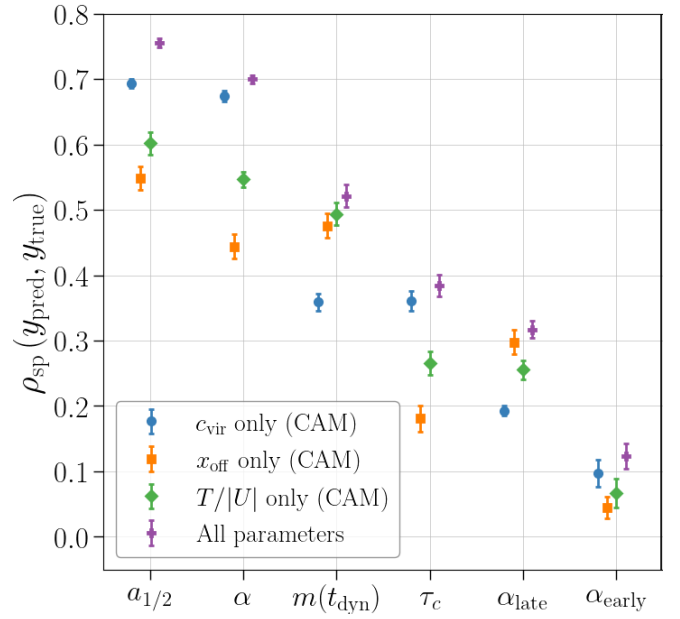


Figure 6. Correlation between MultiCAM predictions of MAH summaries from $z = 0$ halo properties. Here we show the Spearman correlation between parameters characterizing the MAH of haloes in our testing set, and their predictions using the MultiCAM algorithm trained on subsets of the $z = 0$ halo properties. The definitions of these MAH properties can be found in Sections 3.1 and 3.2. The last model (purple cross) corresponds to MultiCAM trained on the following $z = 0$ halo properties: c_{vir} , $V_{\text{max}}/V_{\text{vir}}$, x_{off} , $T/|U|$, λ_{bullock} , and c/a . The correlation from the first three models (blue circle, orange square, and green diamond) is equivalent to the CAM predicted correlation. See Section 4.4 for additional discussion on this figure.

MAH prediction, which outperforms predictions from any individual property. See Fig. 6 and Fig. 7.

DATA AVAILABILITY

The software to reproduce all results in this work is publicly available in Zenodo, at <https://doi.org/10.5281/zenodo.7637864>. Our software is also available at the following public github repository: <https://github.com/ismael-mendoza/multicam>.

The data from the Bolshoi dark matter halo catalogue is publicly available in the CosmoSim data base, at <https://doi.org/10.17876/cosmosim/bolshoi>.

ACKNOWLEDGEMENTS

IM and CA acknowledge support from DOE grant DE-SC009193. IM, KW, and CA acknowledge support from the Leinweber foundation at the University of Michigan. IM acknowledges the support of the Special Interest Group on High Performance Computing (SIGHPC) Computational and Data Science Fellowship. IM acknowledges support from the Michigan Institute for Computational Discovery and Engineering (MICDE) Graduate Fellowship.

This research was supported in part through computational resources and services provided by Advanced Research Computing at the University of Michigan, Ann Arbor. The CosmoSim data base used in this paper is a service by the Leibniz-Institute for Astrophysics Potsdam (AIP). The MultiDark data base was developed in cooperation with the Spanish MultiDark Consolider Project CSD2009-

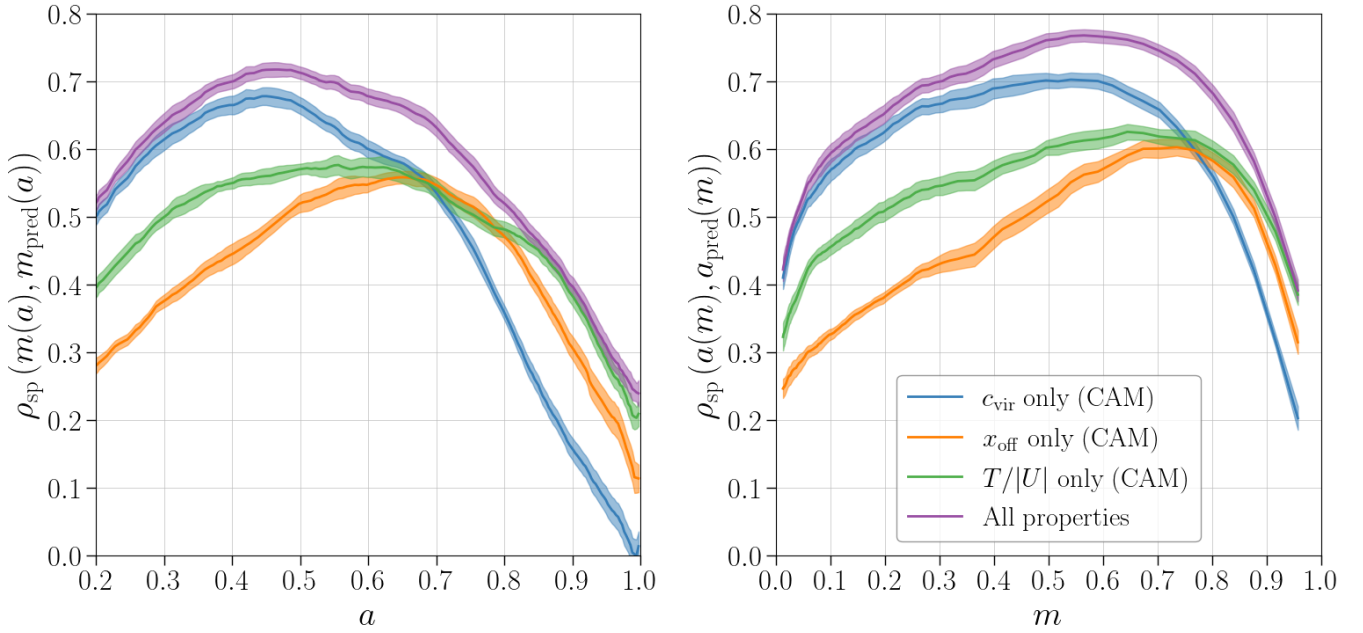


Figure 7. MultiCAM predictions of full MAHs based on $z = 0$ halo properties. Here we use the same models as in Fig. 6 to predict full MAHs, parametrized by $m(a)$ (left) and $a(m)$ (right). The left-hand curves are the Spearman correlations between the predicted $m(a)$ and the true $m(a)$ at each scale a of the Bolshoi simulation starting at $a = 0.2$ for our test set from the M12 data set. Similarly, the right-hand curves are the Spearman correlations between the predicted $a(m)$ and the true $a(m)$ on uniformly spaced log bins on m between 0 and 1. The bands correspond to 68% confidence intervals, estimated by jackknife resampling. See Section 4.4 for additional discussion on this figure.

00064. The authors gratefully acknowledge the Gauss Centre for Supercomputing e.V. (www.gauss-centre.eu) and the Partnership for Advanced Supercomputing in Europe (PRACE, www.prace-ri.eu) for funding the MultiDark simulation project by providing computing time on the GCS Supercomputer SuperMUC at Leibniz Supercomputing Centre (LRZ, www.lrz.de). The Bolshoi simulations have been performed within the Bolshoi project of the University of California High-Performance AstroComputing Center (UC-HiPACC) and were run at the NASA Ames Research Center.

We acknowledge the use of the `scikit-learn` software for linear regression models and quantile transformers (Pedregosa et al. 2011). We also acknowledge the use of `numpy` (Harris et al. 2020), `scipy` (Virtanen et al. 2020), `colossus` (Diemer 2018), `astropy` (Astropy Collaboration 2013, 2018, 2022), `matplotlib` (Hunter 2007), `corner` (Foreman-Mackey 2016), and `lmfit` (Newville et al. 2023).

We thank Andrew Hearin and Daisuke Nagai for feedback on early results of our model and analysis.

REFERENCES

- Allgood B., Flores R. A., Primack J. R., Kravtsov A. V., Wechsler R. H., Faltenbacher A., Bullock J. S., 2006, *MNRAS*, **367**, 1781
- Astropy Collaboration 2013, *A&A*, **558**, A33
- Astropy Collaboration 2018, *AJ*, **156**, 123
- Astropy Collaboration 2022, *ApJ*, **935**, 167
- Behroozi P. S., Wechsler R. H., Wu H.-Y., 2013a, *ApJ*, **762**, 109
- Behroozi P. S., Wechsler R. H., Wu H.-Y., Busha M. T., Klypin A. A., Primack J. R., 2013b, *ApJ*, **763**, 18
- Blumenthal G. R., Faber S., Primack J. R., Rees M. J., 1984, *Nature*, **311**, 517
- Bryan G. L., Norman M. L., 1998, *ApJ*, **495**, 80
- Chen H., Avestruz C., Kravtsov A. V., Lau E. T., Nagai D., 2019, *MNRAS*, **490**, 2380
- Chen Y., Mo H., Li C., Wang H., Yang X., Zhang Y., Wang K., 2020, *ApJ*, **899**, 81
- Cui W., Power C., Borgani S., Knebe A., Lewis G. F., Murante G., Poole G. B., 2017, *Monthly Notices of the Royal Astronomical Society*, **464**, 2502
- Dalal N., Lithwick Y., Kuhlen M., 2010, preprint ([arXiv:1010.2539](https://arxiv.org/abs/1010.2539))
- De Luca F., De Petris M., Yepes G., Cui W., Knebe A., Rasia E., 2021, *Monthly Notices of the Royal Astronomical Society*, **504**, 5383
- Devroye L., 1986, in *Proceedings of the 18th Conference on Winter Simulation*, p. 260
- Diemand J., Moore B., 2011, *Adv. Sci. Lett.*, **4**, 297
- Diemer B., 2018, *ApJS*, **239**, 35
- Diemer B., Kravtsov A. V., 2015, *ApJ*, **799**, 108
- Dunkley J., et al., 2009, *ApJS*, **180**, 306
- Feng Y., Chu M.-Y., Seljak U., McDonald P., 2016, *Monthly Notices of the Royal Astronomical Society*, **463**, 2273
- Foreman-Mackey D., 2016, *J. Open Source Softw.*, **1**, 24
- Freedman D. A., 2009, *Statistical Models: Theory and Practice*. Cambridge University Press
- Frenk C. S., White S. D., 2012, *Ann. Phys.*, **524**, 507
- Gao L., Springel V., White S. D. M., 2005, *MNRAS*, **363**, L66
- Gouin C., Bonnaire T., Aghanim N., 2021, *A&A*, **651**, A56
- Haggar R., Pearce F. R., Gray M. E., Knebe A., Yepes G., 2021, *Monthly Notices of the Royal Astronomical Society*, **502**, 1191
- Harris C. R., et al., 2020, *Nature*, **585**, 357
- Hausen R., Robertson B. E., Zhu H., Gnedin N. Y., Madau P., Schneider E. E., Villaseñor B., Drakos N. E., 2023, *ApJ*, **945**, 122
- Hearin A. P., Watson D. F., 2013, *MNRAS*, **435**, 1313
- Hearin A. P., Watson D. F., Becker M. R., Reyes R., Berlind A. A., Zentner A. R., 2014, *Monthly Notices of the Royal Astronomical Society*, **444**, 729
- Hearin A. P., Zentner A. R., van den Bosch F. C., Campbell D., Tollerud E., 2016, *Monthly Notices of the Royal Astronomical Society*, **460**, 2552
- Hearin A. P., Chaves-Montero J., Becker M. R., Alarcon A., 2021, *Open J. Astrophys.*, **4**, 7
- Hetzner H., Burkert A., 2006, *Monthly Notices of the Royal Astronomical Society*, **370**, 1905
- Horowitz B., Hahn C., Lanusse F., Modi C., Ferraro S., 2022, preprint

(arXiv:2211.03852)
 Hunter J. D., 2007, *Comput. Sci. Eng.*, **9**, 90
 Jespersen C. K., Cranmer M., Melchior P., Ho S., Somerville R. S., Gabrielpil-lai A., 2022, *ApJ*, **941**, 7
 Klypin A. A., Trujillo-Gomez S., Primack J., 2011, *ApJ*, **740**, 102
 Klypin A., Yepes G., Gottlöber S., Prada F., Hess S., 2016, *Monthly Notices of the Royal Astronomical Society*, **457**, 4340
 Knebe A., et al., 2011, *MNRAS*, **415**, 2293
 Kravtsov A. V., Klypin A. A., Khokhlov A. M., 1997, *ApJS*, **111**, 73
 Kravtsov A. V., Berlind A. A., Wechsler R. H., Klypin A. A., Gottlöber S., Allgood B., Primack J. R., 2004, *ApJ*, **609**, 35
 Lau E. T., Hearin A. P., Nagai D., Cappelluti N., 2021, *Monthly Notices of the Royal Astronomical Society*, **500**, 1029
 Lucie-Smith L., Adhikari S., Wechsler R. H., 2022, *MNRAS*, **515**, 2164
 Ludlow A. D., Navarro J. F., Li M., Angulo R. E., Boylan-Kolchin M., Bett P. E., 2012, *Monthly Notices of the Royal Astronomical Society*, **427**, 1322
 Ludlow A. D., et al., 2013, *MNRAS*, **432**, 1103
 Ludlow A. D., Bose S., Angulo R. E., Wang L., Hellwing W. A., Navarro J. F., Cole S., Frenk C. S., 2016, *Monthly Notices of the Royal Astronomical Society*, **460**, 1214
 Maccio A. V., Dutton A. A., Van Den Bosch F. C., Moore B., Potter D., Stadel J., 2007, *Monthly Notices of the Royal Astronomical Society*, **378**, 55
 Machado Poletti Valle L. F., Avestruz C., Barnes D. J., Farahi A., Lau E. T., Nagai D., 2021, *MNRAS*, **507**, 1468
 Mansfield P., Avestruz C., 2021, *MNRAS*, **500**, 3309
 Mantz A. B., Allen S. W., Morris R. G., Schmidt R. W., von der Linden A., Urban O., 2015, *Monthly Notices of the Royal Astronomical Society*, **449**, 199
 Mo H., van den Bosch F. C., White S., 2010, *Galaxy Formation and Evolution*. Cambridge University Press
 Neto A. F., et al., 2007, *Monthly Notices of the Royal Astronomical Society*, **381**, 1450
 Newville M., et al., 2023, *Imfit/Imfit-py: 1.2.1*, doi:10.5281/zenodo.7887568
 Pedregosa F., et al., 2011, *J. Mach. Learn. Res.*, **12**, 2825
 Power C., Knebe A., Knollmann S. R., 2012, *Monthly Notices of the Royal Astronomical Society*, **419**, 1576
 Rey M. P., Pontzen A., Saintonge A., 2019, *MNRAS*, **485**, 1906
 Rodríguez-Puebla A., Behroozi P., Primack J., Klypin A., Lee C., Hellinger D., 2016, *MNRAS*, **462**, 893
 Savitzky A., Golay M. J. E., 1964, *Anal. Chem.*, **36**, 1627
 Sheth R. K., Mo H. J., Tormen G., 2001, *MNRAS*, **323**, 1
 Shin T.-h., Diemer B., 2023, *MNRAS*, **521**, 5570
 Stiskalek R., Bartlett D. J., Desmond H., Anbajagane D., 2022, *MNRAS*, **514**, 4026
 Tashev S., Zaldarriaga M., Eisenstein D. J., 2013, *J. Cosmol. Astropart. Phys.*, **2013**, 036
 Tormen G., Bouchet F. R., White S. D., 1997, *Monthly Notices of the Royal Astronomical Society*, **286**, 865
 Tucci B., Montero-Dorta A. D., Abramo L. R., Sato-Polito G., Artale M. C., 2021, *MNRAS*, **500**, 2777
 Vallés-Pérez D., Planelles S., Monllor-Berbegal Ó., Quilis V., 2023, *MNRAS*, **519**, 6111
 Virtanen P., et al., 2020, *Nature Methods*, **17**, 261
 Vitvitska M., Klypin A. A., Kravtsov A. V., Wechsler R. H., Primack J. R., Bullock J. S., 2002, *ApJ*, **581**, 799
 Wang K., Mao Y.-Y., Zentner A. R., Lange J. U., van den Bosch F. C., Wechsler R. H., 2020, *MNRAS*, **498**, 4450
 Watson D. F., et al., 2015, *MNRAS*, **446**, 651
 Wechsler R. H., Tinker J. L., 2018, *ARA&A*, **56**, 435
 Wechsler R. H., Bullock J. S., Primack J. R., Kravtsov A. V., Dekel A., 2002, *ApJ*, **568**, 52
 White S. D., Rees M. J., 1978, *Monthly Notices of the Royal Astronomical Society*, **183**, 341
 Wong A. W., Taylor J. E., 2012, *ApJ*, **757**, 102
 Zhang B., Cui W., Wang Y., Dave R., DePetrus M., 2022, *Monthly Notices of the Royal Astronomical Society*, **516**, 26
 de Andres D., Yepes G., Sembolini F., Martínez-Muñoz G., Cui W., Rob-

ledo F., Chuang C.-H., Rasia E., 2023, *Monthly Notices of the Royal Astronomical Society*, **518**, 111

APPENDIX A: CONDITIONAL MULTIVARIATE GAUSSIAN SAMPLING ALGORITHM

Let $\mathbf{x} \in \mathbb{R}^m$ be a vector of features and $\mathbf{y} \in \mathbb{R}^\ell$ be a vector of targets. We also assume we have access to a training data set of n pairs: $\{(\mathbf{x}_i, \mathbf{y}_i)\}_{i=1}^n$.

The conditional multivariate Gaussian sampling approach consists of the following steps:

- Assume that \mathbf{x}, \mathbf{y} are jointly Gaussian distributed so that:

$$\begin{bmatrix} \mathbf{y} \\ \mathbf{x} \end{bmatrix} \sim \mathcal{N}(\boldsymbol{\mu}, \boldsymbol{\Sigma}) = \mathcal{N}\left(\begin{bmatrix} \boldsymbol{\mu}_y \\ \boldsymbol{\mu}_x \end{bmatrix}, \begin{bmatrix} \boldsymbol{\Sigma}_{yy} & \boldsymbol{\Sigma}_{yx} \\ \boldsymbol{\Sigma}_{xy} & \boldsymbol{\Sigma}_{xx} \end{bmatrix}\right) \quad (\text{A1})$$

where we separated the mean $\boldsymbol{\mu}$ and covariance matrix $\boldsymbol{\Sigma}$ into corresponding blocks for each variable.

- Empirically compute estimates for the mean $\boldsymbol{\mu}$ and the covariance matrix $\boldsymbol{\Sigma}$ using the training set $\{(\mathbf{x}_i, \mathbf{y}_i)\}_{i=1}^n$. For example:

$$\hat{\boldsymbol{\mu}}_{x,k} = \frac{1}{n} \sum_{i=1}^n x_{ik} \quad (\text{A2})$$

$$\hat{\boldsymbol{\Sigma}}_{xx,k\ell} = \sum_{i=1}^n \frac{(x_{ik} - \hat{\boldsymbol{\mu}}_{x,k})(x_{i\ell} - \hat{\boldsymbol{\mu}}_{x,\ell})}{n-1} \quad (\text{A3})$$

- Given a feature vector in the testing set \mathbf{x}_0 we are interested in obtaining a prediction $\hat{\mathbf{y}}_0$ for the corresponding true target \mathbf{y}_0 . In order to do this we need to determine the conditional distribution $P(\mathbf{y}|\mathbf{x}_0)$.

From statistics we know that the conditional distribution of two or more jointly normal distributed variables is also normal, in particular:

$$\mathbf{y}|\mathbf{x}_0 \sim \mathcal{N}(\bar{\boldsymbol{\mu}}(\mathbf{x}_0), \bar{\boldsymbol{\Sigma}}) \quad (\text{A4})$$

where

$$\bar{\boldsymbol{\mu}}(\mathbf{x}_0) = \boldsymbol{\mu}_y + \boldsymbol{\Sigma}_{yx}\boldsymbol{\Sigma}_{xx}^{-1}(\mathbf{x}_0 - \boldsymbol{\mu}_x) \quad (\text{A5})$$

$$\bar{\boldsymbol{\Sigma}} = \boldsymbol{\Sigma}_{yy} - \boldsymbol{\Sigma}_{yx}\boldsymbol{\Sigma}_{xx}^{-1}\boldsymbol{\Sigma}_{xy} \quad (\text{A6})$$

Note that to calculate this quantities we would replace $\boldsymbol{\mu}$ and $\boldsymbol{\Sigma}$ with their corresponding empirical estimates $\hat{\boldsymbol{\mu}}, \hat{\boldsymbol{\Sigma}}$. Importantly $\bar{\boldsymbol{\mu}}$ depends on a particular test point \mathbf{x}_0 but $\bar{\boldsymbol{\Sigma}}$ does not.

- Finally, from equation (A4) we see that there are two natural options for our predictor $\hat{\mathbf{y}}_0$. We could choose to simply make our predictor the mean of the posterior distribution, i.e., setting $\hat{\mathbf{y}}_0 = \bar{\boldsymbol{\mu}}(\mathbf{x}_0)$. This is reasonable since $\bar{\boldsymbol{\mu}}(\mathbf{x}_0)$ is the most likely value of \mathbf{y}_0 given \mathbf{x}_0 (assuming our statistical model is correct). In fact, in Appendix B we show that this approach is equivalent to linear regression.

Another option is to sample from the distribution in equation (A4) and in this way account for scatter. This is the approach used in Section 3.3.4, and it allows us to accurately capture correlations between target variables. This latter approach is what we refer to as conditional Gaussian sampling.

APPENDIX B: LINEAR REGRESSION: SCATTER AGNOSTIC PREDICTIONS FROM MULTIVARIATE GAUSSIAN

In this short appendix, we will show that the predictions from linear regression and the conditional multivariate Gaussian sampling algorithm in Section 3.3 are equivalent up to the scatter coming from

$\hat{\Sigma}$ (equation A6) in the Gaussian approach. In other words, linear regression outputs the mean of the posterior $P(y|x)$ (equation A4) outputted by the multi-Gaussian approach.

Let $X \in \mathbb{R}^{n \times m}$ be a training data set of features and $Y \in \mathbb{R}^{n \times \ell}$ a training set of predictors. The matrix X contains n training feature vectors each with dimensionality m , and Y contains n predictors each of dimensionality ℓ . Explicitly, the matrices are:

$$X = \begin{bmatrix} \mathbf{x}_1^T \\ \mathbf{x}_2^T \\ \vdots \\ \mathbf{x}_n^T \end{bmatrix},$$

$$Y = \begin{bmatrix} \mathbf{y}_1^T \\ \mathbf{y}_2^T \\ \vdots \\ \mathbf{y}_n^T \end{bmatrix}.$$

For simplicity, we assume that our data set has been mean-centred so that $\hat{\mu}_x = 0$ and $\hat{\mu}_y = 0$ (equation A2).

From standard statistical literature (see, e.g., Freedman 2009), we know that given a new data point $\mathbf{x}_0 \in \mathbb{R}^m$ the linear regression prediction \hat{y}_0 is:

$$\hat{y}_0 = Y^T X (X^T X)^{-1} \mathbf{x}_0. \quad (\text{B1})$$

Let us rewrite the matrix $X^T X$. Given that $X_{ij} = x_{ij}$ we have from equation (A3) that:

$$(X^T X)_{ij} = \sum_k x_{ki} x_{kj} = (\hat{\Sigma}_{xx})_{ij} (n-1), \quad (\text{B2})$$

where the last equality holds since we assumed $\hat{\mu}_x = 0$. Similarly $Y^T X = \hat{\Sigma}_{yx} (n-1)$, so that combining this with equation (B1) we get:

$$\hat{y}_0 = \hat{\Sigma}_{yx} (n-1) \hat{\Sigma}_{xx}^{-1} (n-1)^{-1} \mathbf{x}_0 = \hat{\Sigma}_{yx} \hat{\Sigma}_{xx}^{-1} \mathbf{x}_0, \quad (\text{B3})$$

which is the same as equation (A5) in the mean-centred case. This proves that linear regression is the same as multivariate Gaussian sampling without scatter.

APPENDIX C: MULTICAM CAPTURES COVARIANCES OF PRESENT-DAY HALO PROPERTIES

In Fig. C1, we plot 1D marginals and 2D histograms with 1σ , 2σ , and 3σ contours of our main present-day properties of 3000 haloes from our M12 data set. The orange contours come from the true values of these halo properties and the green contours are samples from MultiCAM (with scatter) applied on the full MAH of each of these 3000 haloes. We overall see good agreement between truth (green) and samples from our model (orange) in both the 1D marginal distributions and the 2D scatter contour plots.

This paper has been typeset from a \LaTeX file prepared by the author.

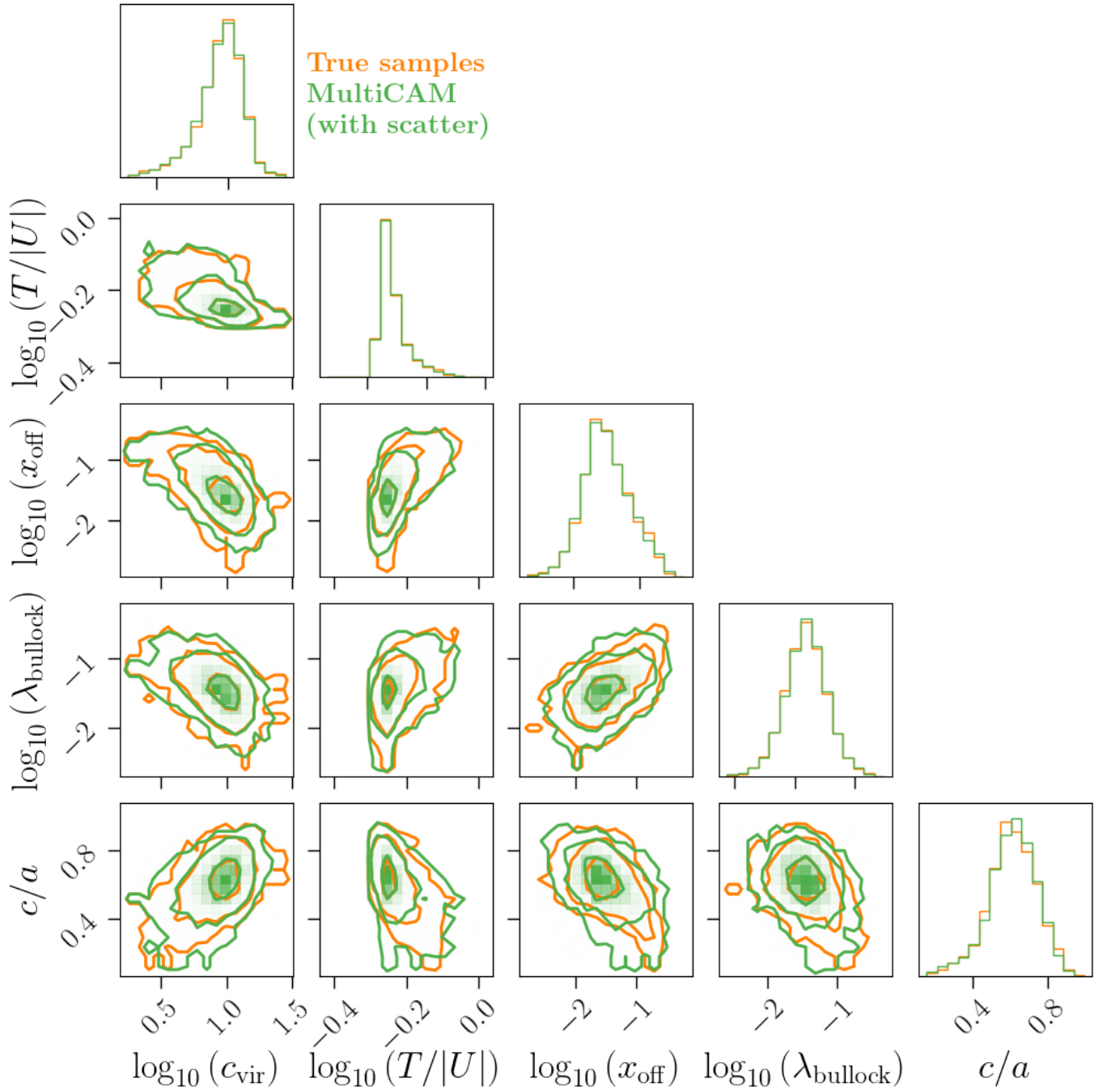


Figure C1. 1D Marginals and 2D Scatter with contours of samples of $z = 0$ halo properties from MultiCAM (with scatter). We show plots of 1D marginals and of 1σ , 2σ , and 3σ contours for the 2D histograms of 3000 samples of $z = 0$ halo properties given their full MAH using MultiCAM (with scatter). The orange contours correspond to a sample of c_{vir} , $T/|U|$, x_{off} , λ_{bullock} , and c/a from 3000 haloes in our M12 data set. The green contours of each subplot were produced by applying MultiCAM (with scatter) on the full MAH of each of the 3000 haloes. See Section 3.3.4 for more discussion on MultiCAM (with scatter). See Appendix C for additional discussion of this figure.